Wide Field Of View Varifocal Near-Eye Display Using See-Through Deformable Membrane Mirrors

David Dunn, *Student Member, IEEE*, Cary Tippets, Kent Torell, Petr Kellnhofer, Kaan Akşit, Piotr Didyk, Karol Myszkowski, David Luebke, *Fellow, IEEE*, and Henry Fuchs, *Life Fellow, IEEE*

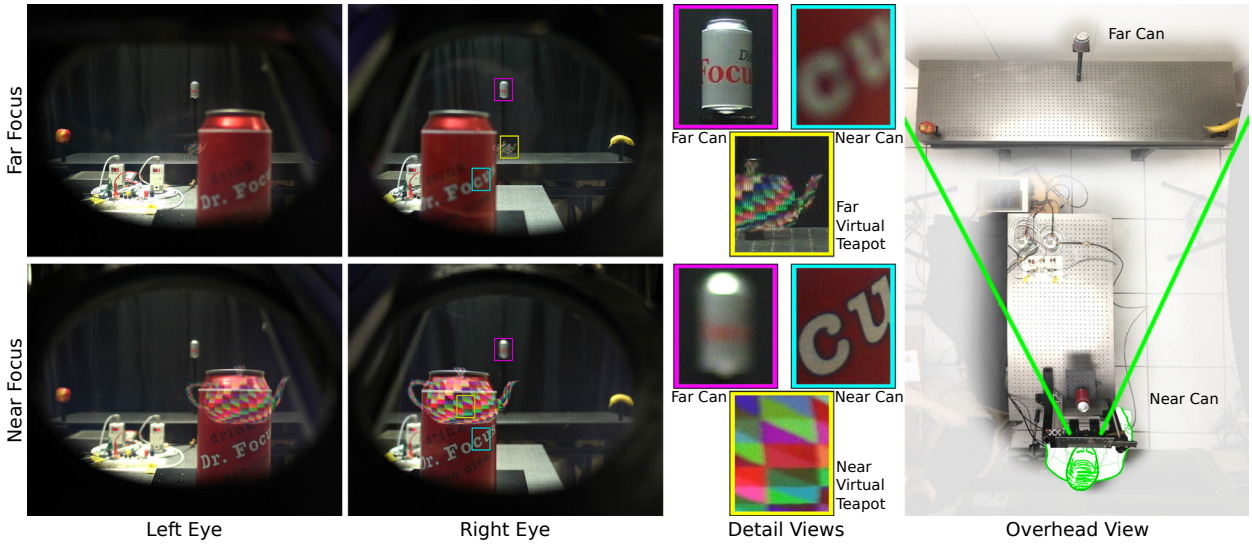

Fig. 1. Wide field of view augmented reality display showing virtual teapot at far and near distance together with real objects, soda cans, at near and far. Photos through display system left and right eyes with focus at far (top row), focus near (bottom row), and overhead view (right) of the system. Details from right eye views showing focus of near and far soda cans and virtual teapot (middle).

Abstract— Accommodative depth cues, a wide field of view, and ever-higher resolutions all present major hardware design challenges for near-eye displays. Optimizing a design to overcome one of these challenges typically leads to a trade-off in the others. We tackle this problem by introducing an all-in-one solution – a new wide field of view, gaze-tracked near-eye display for augmented reality applications. The key component of our solution is the use of a single see-through, varifocal deformable membrane mirror for each eye reflecting a display. They are controlled by airtight cavities and change the effective focal power to present a virtual image at a target depth plane which is determined by the gaze tracker. The benefits of using the membranes include wide field of view (100° diagonal) and fast depth switching (from 20 cm to infinity within 300 ms). Our subjective experiment verifies the prototype and demonstrates its potential benefits for near-eye see-through displays.

Index Terms—Augmented reality, displays, focus accommodation, perception, user study

1 Introduction

Augmented Reality (AR) [7] overlays computer-generated visuals onto the real world in real time. Near-Eye Displays (NEDs) for AR applications have recently been proposed for widespread public use, such as Meta[1], and Microsoft Hololens[2]. Some of the fundamental limitations [23] of existing NEDs for AR are limited field of view (FOV), low angular resolution, and fixed accommodative state.

Computational methodologies such as light fields [14, 24] can provide accommodative cues while enabling wide FOV. However, light field displays are known to be computationally intensive and limited in angular resolution. Always-in-focus methodologies [1, 28] can imitate accommodative cues in computational means, while providing large FOV with a small form factor, but are limited in angular resolution. Varifocal techniques [27, 33] provide high angular resolution and accommodative cues, but none of these systems have achieved a wide FOV up until now. Recent studies show evidence that supporting accommodative cues through a varifocal mechanism improves visual comfort [16] and user performance [33] while being computationally simpler than volumetric displays. Researchers have also proposed several classical optical designs [2, 19, 32, 38] to address only FOV-related issues without addressing accommodative cues related issues. As demonstrated by Benko et al. [3], combining a NED with projections

- *David Dunn is with UNC Chapel Hill, E-mail: dunn@unc.edu.*
- *Cary Tippets is with UNC Chapel Hill, E-mail: tippetsc@ad.unc.edu.*
- *Kent Torell is with UNC Chapel Hill, E-mail: torell@live.unc.edu.*
- *Petr Kellnhofer is with MPI Informatik, E-mail: pkellnho@mpi-inf.mpg.de.*
- *Kaan Akşit is with NVIDIA Research, E-mail: kaksit@nvidia.com.*
- *Piotr Didyk is with MMCI at Saarland University, E-mail: pdidyk@mmci.uni-saarland.de.*
- *Karol Myszkowski is with MPI Informatik, E-mail: karol@mpi-inf.mpg.de.*
- *David Luebke is with NVIDIA Research, E-mail: dluebke@nvidia.com.*
- *Henry Fuchs is with UNC Chapel Hill, E-mail: fuchs@cs.unc.edu*

Manuscript received 19 Sept. 2016; accepted 10 Jan. 2017.
Date of publication 26 Jan. 2017; date of current version 18 Mar. 2017.
For information on obtaining reprints of this article, please send e-mail to: reprints@ieee.org, and reference the Digital Object Identifier below.
Digital Object Identifier no. 10.1109/TVCG.2017.2657058

[1] https://www.metavision.com/
[2] http://www.microsoft.com/microsoft-hololens/en-us

Table 1. Comparison of Near-Eye Displays That Enable Accommodative Cues.

	Focus mechanism	See-through	FOV	Angular resolution	Optics	Form factor	Computational demand
Free-form optics [13]	light fields	yes	small	high	complex	moderate	high
Near-eye light field displays [24]	light fields	no	small	low	simple	thin	high
Light field stereoscope [14]	light fields	no	large	low	simple	moderate	high
Pinlight displays [28]	always-in-focus	yes	large	low	simple	thin	moderate
Pinhole displays [1]	always-in-focus	no	large	low	simple	thin	moderate
Holographic optical elements [18]	holographic	yes	N/A	N/A	complex	N/A	high
Multi-focal plane displays [12]	multi-plane	yes	small	high	complex	bulky	high
Focus tunable light engine [27]	varifocal	yes	small	high	moderate	N/A	N/A
Focus tunable lenses [33]	varifocal	no	small	moderate	moderate	moderate	moderate
This work	varifocal	yes	large	moderate	simple	bulky	moderate

promises larger FOV with no accommodative cues, but it introduces new practical challenges.

In this paper, we tackle the problem of providing wide FOV and accommodative cues together in the context of see-through and varifocal systems. By bringing the idea of hyperbolic half-silvered mirrors [19] and deformable membrane mirrors [30,31,34] together for NEDs in AR applications, we propose a new hybrid hardware design for NEDs that uses see-through deformable membrane mirrors. We present a complete prototype that promises to address Vergence-Accommodation Conflict (VAC) [11] caused by lack of accommodative cues. We validate the performance of our accommodation control in a subjective experiment.

1.1 Contributions

Single Element Optics: Our design employs a single optical element as the varifocal relay optics, simplifying the design of see-through varifocal optical systems for NEDs in AR applications. We present a ray tracing model for exploring the design space of our proposal.

Wide Field Of View: With respect to other varifocal optical components, our optical element is unique due to its large aperture size, leading to wide FOV NED solutions for AR applications. We present different design scenarios leading to wide FOV, accurate defocus blur, and demonstrate a wide FOV prototype.

Vergence-Accommodation Conflict: We verify our gaze tracked prototype through a subjective test. Our findings indicate the ability to address Vergence-Accommodation Conflict (VAC) in a gaze-driven way.

Complete Prototype: As a proof of concept, we demonstrate a binocular varifocal NED prototype with gaze tracking capability, created by modifying off-the-shelf items, and in-house custom built deformable see-through mirrors. We provide details of our implementation.

Unlike for other methodologies, the computational requirements of image generation for a varifocal system are almost the same as today's conventional NEDs. Thus, we believe a varifocal system is very likely to be a design choice in next generation NEDs. We hope our easy-to-follow manufacturing and implementation processes provide a reproducible methodology for researchers and manufacturers.

2 Related Work

Enabling accommodative cues is known to cause major changes in a NED's optical design. We revise the designs that have enabled accommodative cues, investigate their characteristics, and provide a comparison of these solutions in Table .

Integral Imaging, first proposed by Lippmann [26], deals with the capture and the reproduction of light fields which with enough angular resolution can provide correct accommodative cues to a viewer. Hua and Javidi [13] demonstrate a NED for AR applications that combines recent advancements of free-form relay optics with a computational integral imaging methodology, achieving 15° of diagonal FOV with a maximum image resolution of 640×360 px, leading to $10-20$ cpd. Although rendering of images is instant, the free-form optics in their design use 3 different 10th order polynomial lenses made of Polymethyl methacrylate (PMMA), which requires an access to precision machinery for replication of the work.

Lanman and Luebke [24] introduce a Near-Eye Light Field Display (NELD) that uses microlenses as the relay optics, showing a prototype with a screen of 146×78 px and a FOV of $29.2° \times 16.0°$, leading to a resolution of $2-3$ cpd. More recently, Huang et al. [14] developed NELDs for virtual reality (VR) applications further, demonstrating a light field stereoscope with a diagonal FOV of 110°, an accommodation range of 5.26 to 0.81 diopters, and a maximum image resolution of 640×800 px ($3-4$ cpd). The prototype from Huang et al. employs two Liquid Crystal Displays (LCDs) and a pair of classical magnifiers. The introduced technique also promises a continuous depth information with a computational overhead that demands usage of high-end GPUs, and presents online images at a typical rate of $20-35$ fps. Always-in-focus mechanisms also offer sharp imagery across different focal planes. The work of Akşit et al. [1] uses a pinhole mask in front of a display as a NED for VR applications, and demonstrates full color images at a diagonal FOV of 83° with a resolution of 460×260 px ($2-3$ cpd). The "Pinlights" always-in-focus AR display, by using a see-through sparse backlight mechanism from Maimone et al. [28], introduces a single color prototype with a diagonal FOV of 110°, and a resolution of $2-3$ cpd. The work of Maimone et al. can also provide full-color imagery with 12 Hz refresh rate. Both of these implementations suffer the primary disadvantage of poor angular resolution.

Researchers have shown a growing interest in the use of Holographic Optical Elements (HOEs) in NED designs [18]. Holography promises a good angular resolution with a thin form factor, but to our knowledge, no implementation of HOEs inside a complete NED has yet been demonstrated. We believe high FOV will be the major practical challenge in holographic NED research.

The work of Hu and Hua [12] presents a see-through multi-plane NED using Deformable Mirror Membrane Devices (DMMDs) that provide 1 kHz refresh rate. Their prototype provides a 40° diagonal FOV, and an image resolution of 1024×768 px, leading to resolvability of $9-12$ cpd. However, the optical complexity in such approaches has to date challenged their practicality in increasing angular resolution and decreasing form factors.

Closely related to our proposal, a varifocal system by Liu et al. [27] uses a tunable lens system combined with a spherical mirror, and demonstrates 28° of diagonal FOV, 800×600 px resolution ($10-$

14 cpd), and an accommodation range of 0 to 8 diopters. The work of Liu et al. switches depth from one extreme to an another within 74 ms (108 diopters per second). A recent study by Konrad et al. [33] again takes advantage of an electrically tunable lens system as relay optics and demonstrates 36° diagonal FOV. Their solution switches depth from one extreme to an another within 15 ms (600 diopters per second), and provides a maximum image resolution of 488×488 px (5 – 6 cpd) and an accommodation range of 9.5 – 0 diopters. Konrad et al. also propose an interesting drive scenario through monovision. A detailed perceptual study on monovision was also conducted recently by Johnson et al. [15].

A more comprehensive review can be found in the work of Kramida et al [22]. To our knowledge, our proposal is the first approach promising a see-through single element varifocal NED with wide FOV and improved angular resolution.

3 System Overview

The goal of a varifocal see-through NED is to place a virtual image at a variable focal distance from a human subject's eyes. We approach the problem of designing optics for a see-through NED with a layout shown in Figure 2. A display located above a user's eye is reflected from a deformable membrane mirror towards the user. Assuming a mechanism causing a uniform deflection of the membrane, the deformable membrane mirror approximates a spherical concave reflective surface, defined as

$$(x-x_0)^2+(y-y_0)^2+(z-z_0)^2=r^2, \tag{1}$$

where (x,y,z) defines the points on the sphere surface, $M_c=(x_0,y_0,z_0)$ defines the coordinates of the sphere center, and r defines the radius of the curvature. As a result of the deflection, the user perceives the virtual image at different focal distances that depend on the mirror curvature.

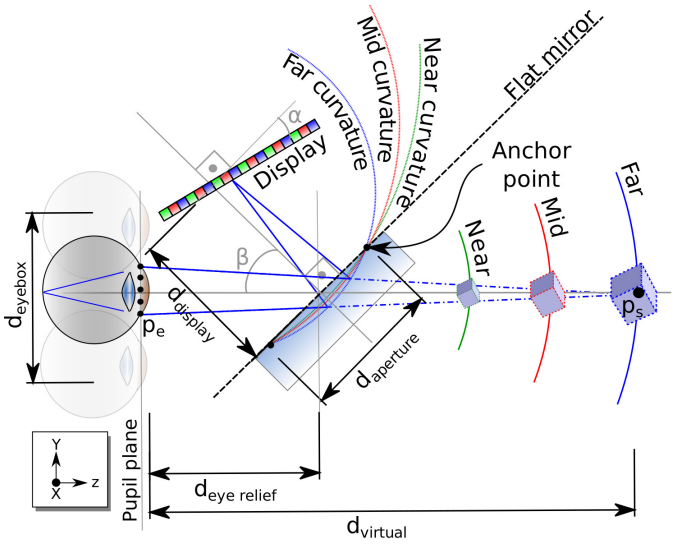

Fig. 2. A sketch showing our varifocal optical layout with parameters for the single eye case. An image on a display above the user's eye reflects from our deformable membrane mirror toward the eye. A virtual image can be created at a desired position in space by varying the curvature of our deformable membrane mirror.

We start our design (Figure 2) by placing a flat membrane in front of an eye with a certain eye relief $d_{eye\ relief}$ and aperture size $d_{aperture}$. We tilt the membrane with an angle β around the X axis. We then place the display at a distance $d_{display}$ from the membrane, and tilt it with an angle α. Desired eye-box size, $d_{eye\ box}$, and $d_{aperture}, d_{eye\ relief}, \alpha, \beta, d_{display}$ are parameters of our design.

3.1 Ray tracing model

We approached the problem of calculating the required mirror curvatures for a given configuration through a three-dimensional (3D) ray tracing model [39]. The objective of our ray tracing model is to find a good mirror curvature that creates the smallest resolvable spot size. The first step of our model defines sample points p_e inside a given $d_{eye\ box}$. In our ray tracing routine, all sample points from a given $d_{eye\ box}$ collectively represents a forward gazing eye aperture aligned with the optical axis (Z axis). Next, we define a sample point p_s at a desired depth $d_{virtual}$. We choose a p_s aligned with the optical axis again. We define multiple rays from points inside p_e an eye box traveling to a sample point p_s in depth. A single one of these rays R_0 is defined as

$$R_0=\begin{cases} p_e=\begin{bmatrix} p_{e_x}\\ p_{e_y}\\ p_{e_z}\end{bmatrix}, \\ a_{es}=\frac{1}{d_{es}}\begin{bmatrix} p_{s_x}-p_{e_x}\\ p_{s_y}-p_{e_y}\\ p_{s_z}-p_{e_z}\end{bmatrix}, \end{cases} \tag{2}$$

where p_e indicates a starting point, a_{es} indicates direction cosines of the ray, and d_{es} indicates the distance between p_e and p_s. We trace R_0 from pupil plane to deformable membrane mirror. Note that Figure 2 shows two anchor points for the deformable membrane mirror. Any given sphere that has such anchor points at both axis (X and Y) by definition is on the line that is perpendicular to the flat mirror surface, and crosses the center of the flat mirror surface. Assuming a configuration as in Figure 2, such a line can be defined as $z=-tan(\beta)(y+d_{eye\ relief})$, leading to $M_c=(0,y,z)$. The intersection point between a deformable membrane and R_0 can be calculated by finding a ray propagation distance d_0 that satisfies the sphere equation on the surface of the membrane with a point $p_{mirror}=(p_e+d_0\ a_{es})$. Thus, ray propagation distance can be calculated by finding the roots of

$$\|p_{mirror}-M_c\|=r, \tag{3}$$

and choosing the closest root to the plane of the deformable membrane mirror. A surface normal R_{n_0} of the deformable membrane mirror at a point can be calculated as

$$R_{n_0}=\begin{cases} n_{mirror}=p_{mirror}, \\ a_{mirror}=\frac{p_{mirror}-M_c}{\|p_{mirror}-M_c\|}. \end{cases} \tag{4}$$

Using R_{n_0} and R_0, we calculate the reflection as a ray R_1 which can be calculated as

$$R_1=R_0-2R_{n_0}(R_0\cdot R_{n_0}). \tag{5}$$

To calculate the intersection of R_1 with a display plane, we need to be able to calculate two things: (1) surface normal of our display plane and (2) ray propagation distance d_1 from the origin of the ray to a display plane. The surface normal of our display plane R_{n_1} can be calculated as

$$R_{n_1}=\begin{cases} p_{display}=\begin{bmatrix} 0\\ sin(\beta)\ d_{display}\\ d_{eye\ relief}-cos(\beta)\ d_{display}\end{bmatrix}, \\ a_{display}=\begin{bmatrix} 0\\ sin(\beta+\alpha)\\ cos(\beta+\alpha)\end{bmatrix} \end{cases}. \tag{6}$$

Using the surface normal and a vector R_2 from p_{mirror} to $p_{display}$, d_1 can be calculated as

$$d_1=\frac{R_{n_1}\cdot R_2}{R_{n_1}\cdot R_1}, \tag{7}$$

and finally, we can find the intersection point as $p_{final}=p_{mirror}+d_1\ a_{R_1}$. We use the intersection points to calculate the spot size, in

which Full Width Half Maximum (FWHM) size of the spot diagonal is calculated using $FWHM = 2.355\sigma$. Using secant method, we optimize the curvature of the deformable mirror membrane by minimizing FWHM size for a given configuration. We choose a new curvature r_{new} at each iteration as

$$r_{new} = r_{current}\left(1 - \frac{FHWM_{current} - FWHM_{previous}}{r_{current} - r_{previous}}\right). \quad (8)$$

3.2 Design space

Here we explore the design space of our proposal using our ray tracing model to identify the impact of $d_{eye\ relief}$, $d_{display}$, and $d_{aperture}$. First, we will analyze $d_{aperture}$, which is defined both in the vertical and the horizontal axis. In our designs, the aperture shapes are chosen as either circular or elliptical. Adult humans have a mean interpupillary distance (IPD) of 63 *mm*, and their IPDs can range between 50 and 75 *mm* [8]. Thus, horizontal aperture size is dictated by IPD in the nasal direction. Maximum aperture size at a vertical axis can be of any desired size to cover a larger vertical FOV. Note that user's eyes can be decentered with respect to the optical axis of a deformable membrane mirror; thus we choose to use $d_{eye\ box} = 20$ *mm* to compensate for alignment as in the case of a conventional NED design. Designs with elliptical aperture shapes can introduce perceptible astigmatism in an optical system. Such cases can easily be corrected by placing a single axis lens in between a display and a deformable membrane mirror.

Sample designs in Figure 3 demonstrate our findings on the effects of $d_{eye\ relief}$ and $d_{aperture}$ on FOV. These results suggest that shorter $d_{eye\ relief}$ and larger $d_{aperture}$ promise a larger FOV. We would like to highlight that majority of our designs promise a larger FOV than a typical NED for AR applications. The main limitation of our designs comes from the limited FOV generation towards the brows due to the β angle of the membrane mirror causing a more distant reflector in that region. Note that an asymmetrical aperture in different directions (brow, nose, cheek, peripheral), different aperture shapes (square, custom) or offsetting and angling the central axis of the membrane are possible solutions to overcome limited FOV towards the nose and the brow. However, non-elliptical designs require a more complex multi-domain modeling, leading to complex surface deformations largely deviating from regular spherical or aspherical surfaces, while off-axis designs degrade the optical qualities of the reflected image. Increasing the aperture size will also lead to clipping the reflections of the display particularly in the bottom region which reflects the portion of the display that abuts the brow.

We propose a pneumatic system to control the deformations of the membrane mirror. Understanding the required curvature values and maximum displacement for a deformable membrane mirror lets us identify the speed and volume of air movement that dictated the requirements for the pneumatic hardware. We explore the impact of different $d_{eye\ relief}$ and $d_{aperture}$ on curvature, displacement, and resolution by ray tracing to simulate the characteristics of different points in depth aligned with the optical axis. Our ray tracing model suggests that different $d_{eye\ relief}$ leads to different M_c, and r configurations meaning the deformable membrane displaces different amounts with respect to the flat mirror case. We show the effect of $d_{eye\ relief}$ with a sample design in Figure 4. Note that shorter $d_{eye\ relief}$ requires less deformation of the deformable membrane mirror, which, as a result, requires more precise pneumatics. On the other hand, larger $d_{eye\ relief}$ provides a smaller resolvable pixel size, leading to more resolution, but as noted above decreases the FOV. We conclude the pixel size dictates the required $d_{eye\ relief}$ in practical designs. We also evaluate the same sample designs for different $d_{display}$, as shown in Figure 5. This shows that larger $d_{display}$ increases resolution while decreasing the required amount of deformation on the membrane, but also increases the overall form factor of the complete system while decreasing FOV.

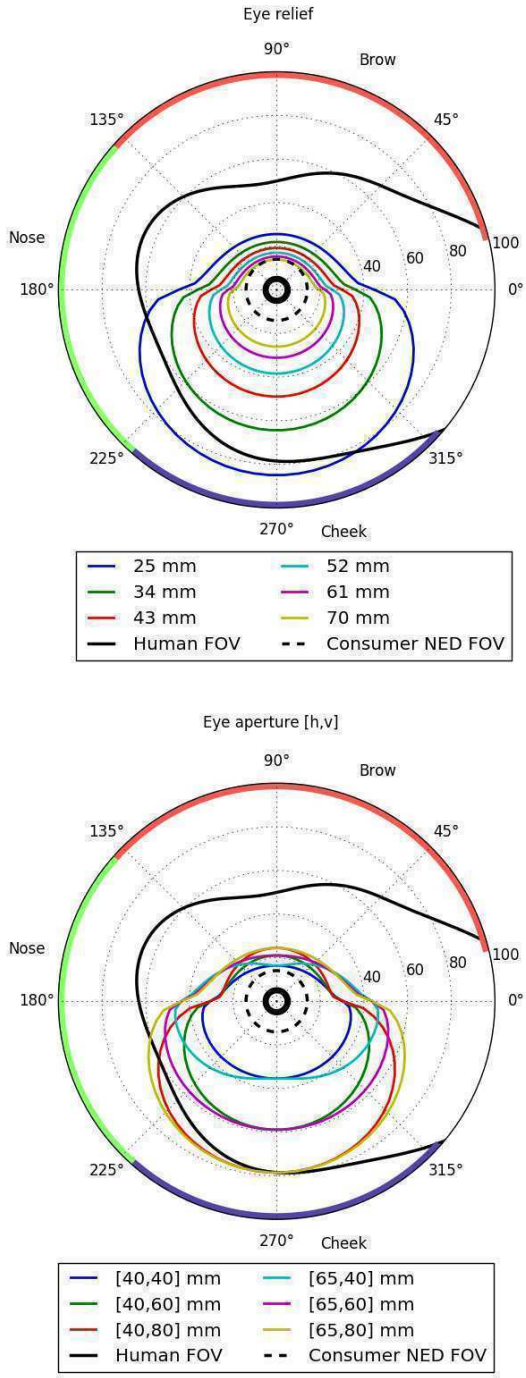

Fig. 3. Perimetric charts in degrees showing calculated visible FOV of different sample designs for a right eye of a user while gazing statically forward. In both sketches, the solid black line represents an average FOV of a person, the solid small black circle represents foveal region, and the dashed black line represents FOV of a typical consumer level NED for augmented reality applications. Angular positions of facial features are highlighted as brow, nose, and cheek. The top figure shows variation of FOV for different values of eye relief $d_{eye\ relief}$. Calculations are based on a vertical aperture size $d_{aperture_v} = 65$ *mm*, a horizontal aperture size $d_{aperture_h} = 50$ *mm*, and deformable membrane mirror tilt $\beta = 45^o$. The bottom figure shows variation of FOV for different values $d_{aperture_v}$, and $d_{aperture_h}$. Calculated values in the bottom figure are based on $d_{eye\ relief} = 34$ *mm*, and $\beta = 45^o$.

4 Implementation

We demonstrate our proposal with an experimental see-through varifocal NED equipped with a gaze tracker as shown in Figure 6. All the hardware components used in our final prototype are presented in a

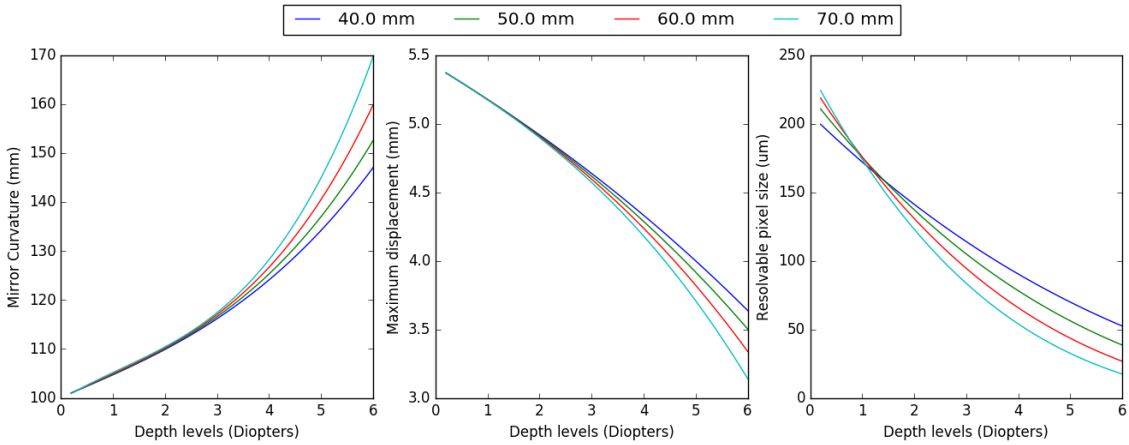

Fig. 4. A sample design is evaluated for different eye reliefs $d_{eye\ relief}$ with a configuration of an aperture size $d_{aperture} = 50$ mm in horizontal axis, an aperture size $d_{aperture} = 65$ mm in vertical axis, a mirror tilt $\beta = 45°$, a screen tilt $\alpha = 20°$, an eye box $d_{eye\ box} = 20$ mm, and a screen distance $d_{display} = 60$ mm. For all evaluations, on-axis depth fields as shown in Figure 2 are chosen at different depth levels. A deformable membrane mirror's curvature is calculated for different depth levels as shown on the left. The maximum amount of displacement required by each depth level is shown in the middle figure. Assuming an eye with an aperture size of 6 mm, resolvable pixel size on a screen inside the given eye box is calculated for different depth levels as shown in the figure on the right. Smaller $d_{eye\ relief}$ benefits the design by decreasing required displacement on a membrane, however resolution improves at closer depths with a larger $d_{eye\ relief}$.

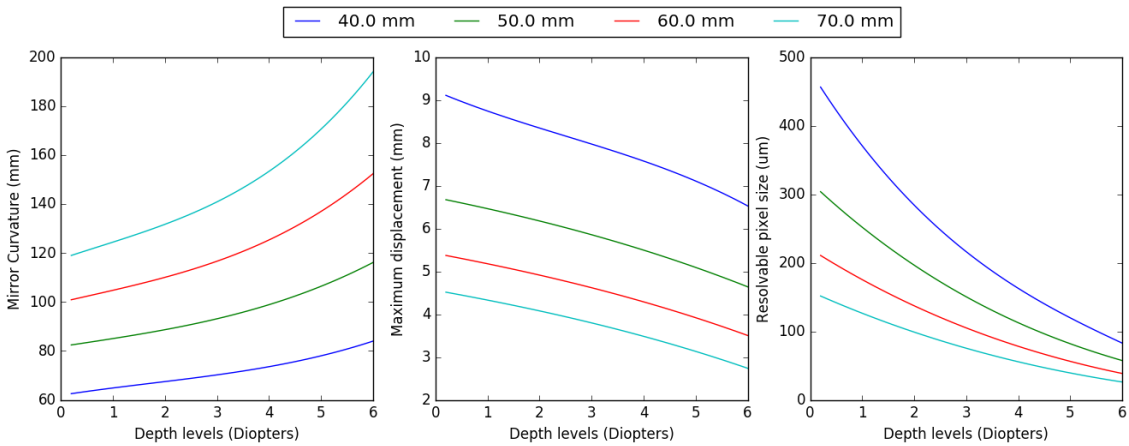

Fig. 5. A sample design is evaluated for different display distances $d_{display}$ with a configuration of an aperture size $d_{aperture} = 50$ mm in horizontal axis, an aperture size $d_{aperture} = 65$ mm in vertical axis, a mirror tilt $\beta = 45°$, a screen tilt $\alpha = 20°$, an eye box $d_{eye\ box} = 20$ mm, and a eye relief $d_{eye\ relief} = 50$ mm. For all evaluations, on-axis depth fields as shown in Figure 2 are chosen at different depth levels. A deformable membrane mirror's curvature is calculated for different depth levels as shown on the left. The maximum amount of displacement required by each depth level is shown in the middle figure. Assuming an eye with an aperture size of 6 mm, resolvable pixel size on a screen inside the given eye box is calculated for different depth levels as in the figure on the right.

system overview diagram as in Figure 7.

In this section, we explain details of our implementation. The core of our proposal and the only custom component is a deformable membrane mirror and its vacuum-tight 3D-printed housing.

4.1 Manufacturing flexible membranes

The task of manufacturing custom flexible membranes is accomplished traditionally through surface micromachining, bulk micromachining, liquid crystals, piezoelectric or electrostrictive actuators as reviewed by Mansell et al. [29]. Pneumatic based systems have also been demonstrated for building tunable microoptics using polydimethysiloxane (PMDS) [42], avoiding the use of high voltages or external fields in operation and precise machining in manufacturing. On the other hand, PDMS has numerous attractive material properties such as outstanding transparency in visible wavelengths, high elasticity, and excellent temperature stability. Inspired by these advantages, we created our own recipe for the task.

We used Sylgard 184 PDMS kit purchased from Dow Corning. Sylgard 184 is a two-part elastomer kit, with PDMS pre-polymer and a cross-linking agent. The prepolymer was mixed with cross-linking agent at a ratio of 10 : 1 and mixed vigorously for 3 minutes. The mixture was then degassed for 15 minutes, to remove bubbles incorporated during mixing. 6" Silicon wafers were purchased from University Wafers. The Wafer was silanized, to ease membrane release, by being placed in a desiccator, with 20 ul of trichloro (1H,1H,2H,2H-perfluorooctyl) silane and evacuated for 30 minutes and left under vacuum for 1 hour. Mixed and degassed PDMS prepolymer is spin cast on the Si wafer for 1 min at 300 RPMs to obtain a PDMS membrane of approximately 240 um. The membrane is placed in an oven at 100° C for 24 hours to produce a repeatable Young's modulus [37]. The membrane was then placed in a commercial physical vapor deposition unit (Kurt Lesker PVD 75) and a 20 nm Ag film is sputtered on the membrane. After metalization the film is carefully peeled and stretched taut across the vacuum housing to form the deformable membrane mirror. Fused Deposition Modeling (FDM) based 3D printers that we have tried were not able to accomplish the task of manufacturing

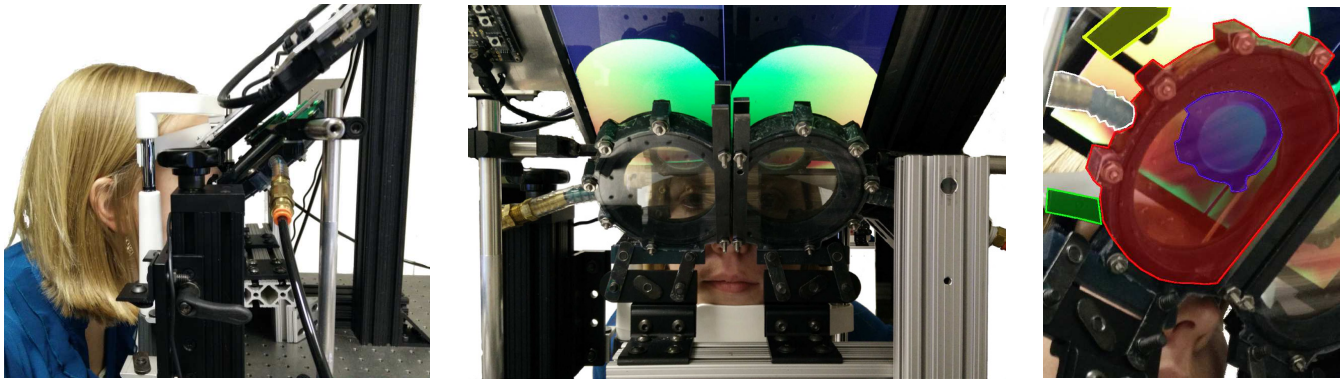

Side view Front view Bottom view

Fig. 6. Photographs showing side, front, and bottom views of our wide field of view varifocal near-eye display prototype for Augmented Reality applications. Bottom view presents red, blue, green, yellow, and white highlighted regions, which are the deformable membrane mirror for right eye, an additional lens to overcome astigmatism in the central regions caused by elliptical deformable membrane aperture shape, a infra red camera for deformation control, a camera for gaze tracking, and a pneumatics connection to the 3D printed deformable membrane mirror housing.

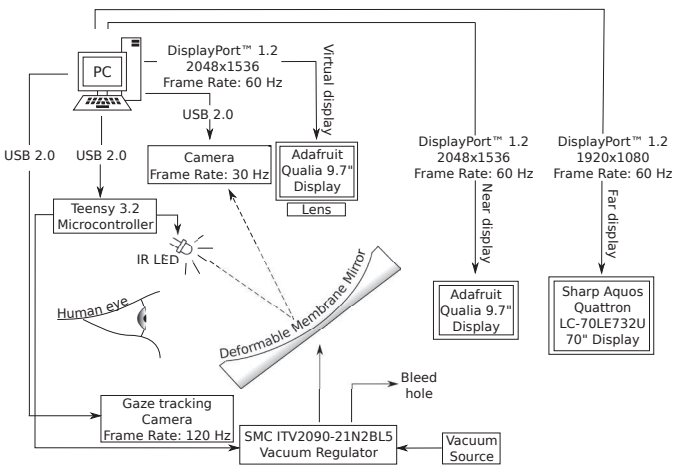

Fig. 7. A sketch showing the system overview and connections of the hardware in our prototype.

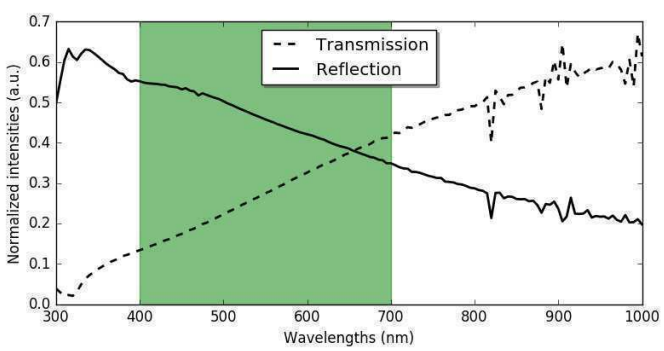

Fig. 8. Figure showing the wavelength dependent transmission and reflection characteristics of the in-house manufactured deformable membrane. Green highlighted region corresponds to visible wavelengths.

airtight vacuum housing. We manufactured the housing using a Formlabs 2 3D printer[3], which uses stereolithography technique with liquid photopolymer resins.

Transmission and Reflection characteristics of our deformable membrane mirror were captured as in Figure 8 using a J. A. Woollam variable angle spectroscopic ellipsometer. The deformable membrane mirror was aligned and the incident angle was set to 40 degrees to match β and α for both the transmission and reflection measurements. Work of Lee et al. [25] highlights that a thickness of an optical combiner plays a crucial role in depth perception, as our membrane mirror has 240 μm thickness, effects described by Lee et al. are expected to be at a negligible level in our implementation.

4.2 Integration

Our choice of design parameters was mainly constrained by the availability of off-the-shelf components and the costs of custom tooling. Per eye, we use a vacuum source (115 Torr $\sim$ 15 kPa) with a SMC ITV2090-21N2BL5[4] vacuum regulator, a t-junction, and a bleed hole to create a controlled partial vacuum environment inside our vacuum housing. Our vacuum regulators can regulate pressure levels in between -1.3 to -80 kPa, and each is controlled by a Teensy 3.2 microcontroller[5] (μC). Our combination of μCs and vacuum regulators provides us $\sim$ 60 addressable stable depth planes ranging from 0.2 to 7 diopters according to our empirical experiments. We used a Adafruit Qualia 9.7″ LCD[6] with 260 ppi, active region used per eye is 1050×1260 px. Our prototype uses a gaze tracking Pupil-labs camera[7] per eye, running at 120 Hz.

Given the components and the evaluated sample designs, we chose the following design parameters: $d_{eye\ relief} = 65$ mm, $\beta = 40°$, $\alpha = 10°$, $d_{aperture} = 65.5 \times 80.7$ mm (H×V), and $d_{display} = 45$ mm. Our fully assembled prototype is shown in Figure 6. FOV provided by our prototype matches our estimations computed using ray-tracing model. Monocular FOV and binocular FOV of our prototype are measured as 60°H and 90°H×45°V, respectively. We used an additional single axis lens in front of the central regions of our display to minimize astigmatism caused by elliptical aperture choice.

Using an early prototype of the housing, we conducted a deformation test for our deformable membrane mirror as shown in Figure 9. During our deformation tests, we stressed the membrane to deformations that are 10 times larger than the deformations that we have during operation. Large ripples at the edge of the deformable membrane are believed to be caused by a weak attachment to the housing wearing out after 26700 iterations, which we solved in later iterations of the housing with a more secure attachment. Hazing in the images is believed to be caused by a change in surface structure after many iterations. Our deformation test was conducted over a 30 hour time frame. As our membrane underwent strains far greater than during normal operation

[3]http://formlabs.com/

[4]https://www.smcpneumatics.com

[5]https://www.adafruit.com/product/2756

[6]https://www.adafruit.com/product/1652

[7]https://pupil-labs.com/store/

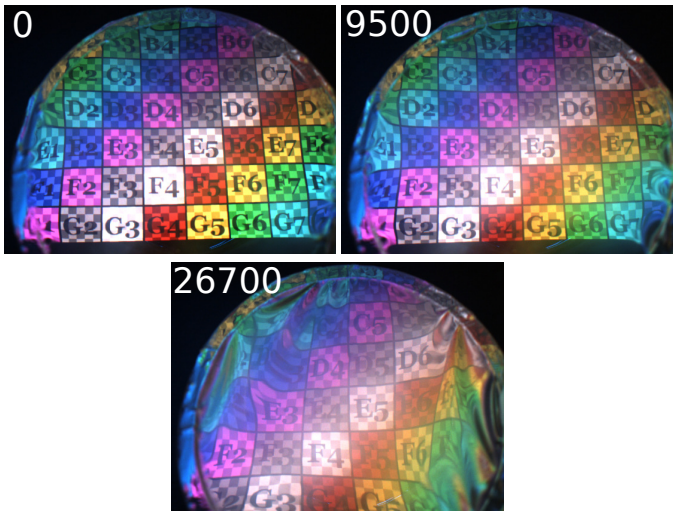

Fig. 9. Photographs showing the result of our deformation test to estimate usability over lifetime for our in-house built deformable membrane mirror. We iterate on stretching the deformable membrane mirror back and forth with 10 times larger deformations than we use during operation. Each photograph shows a counter that represents number of iterations.

without failing, we can conclude that our deformable membrane mirror and pneumatics control mechanism are suitable for long term usage.

4.3 Software

We developed an in-house software to control our prototype, to conduct subjective experiments, and to render images accordingly. Our software is written in Python programming language taking advantage of GLFW[8] for user interface rendering, OpenCV[9] for image processing tasks, and Pupil-labs library for gaze tracking tasks. Our software runs on an Intel Xeon CPU W5590 @ 3.33 GHz PC with two Nvidia Quadro NVS 420 GPUs and Linux operating system.

Our control methodology for the deformations of the deformable membrane mirror is based on reflection shape detection from an Infra-Red (IR) Light Emitting Diode (LED) placed above each deformable membrane mirror. An IR camera running at 30 FPS for each deformable membrane mirror is also placed above the deformable membrane mirror as shown in bottom view of Figure 6. Whenever, system is dictated to change the effective focal power, PC electronically controls the vacuum regulator through uCs, and reflection detections from IR cameras act as a feedback mechanism to form a closed loop control mechanism.

For different depth levels, image distortions caused by our deformable membrane mirror are captured by a PointGrey Flea FLEA-HICOL camera[10] with a Fujinon $F1:1.2-2.8-8$ mm aperture lens. Note that the mentioned camera is for identification of image distortions, and not a permanent part of our system. We characterized image distortions by using the work of Yamazaki et al. [43] and our captures. We applied our findings on the image distortions to our software to present images consistently with the changing focus.

5 Experiments

The goal of our experiment was to verify whether our accommodation support works well, and if users can benefit from it while performing visual acuity task in a monocular viewing scenario. Our hypothesis was that a correct accommodation will allow users to resolve higher spatial details.

[8]http://www.glfw.org/
[9]http://opencv.org/
[10]https://www.ptgrey.com

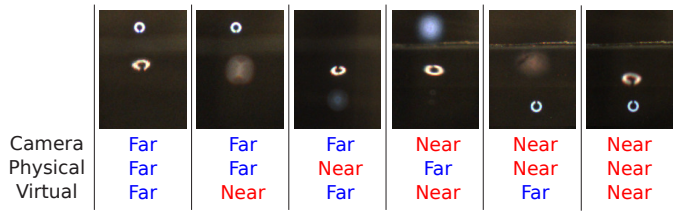

Fig. 10. Series of photographs showing example stimulus as seen by a participant during our experiment. Labels below each photograph indicates focal state of our camera, physical location of the display, and the depth of the virtual image.

5.1 Stimuli

Each stimulus consisted of a pair of white Landolt C shapes shown on a black background (Figure 10). The location of the gaps was either on the top or the bottom side corresponding to the up and the down orientation of the shape. The shapes were separated by 2 visual degrees, and each of them spanned 30 arcmin which imposes the gap size of 6 arcmin, where the normal 20/20 eye can resolve 1 arcmin. Since through our NED calibration its focus state has been precisely setup for each trial, we opted for the larger gap size so that the user response is immediate and effortless, as well as it is not affected by lower display contrast, limited spatial resolution, and possibly imperfect luminance adaptation with respect to the requirements of standard visual acuity test. One shape was presented on one of two physical screens located at 0.25 m (Adafruit Qualia, $9.7''$, 2048×1536, 23.5 cpd, 60 Hz) and 5.0 m (Sharp Aquos Quattron LC-70LE732U, $70''$, 1920×1080, 54.3 cpd, 60 Hz) from the viewer. The other Landolt shape was presented on our NED with a focal distance either matching the distance to the physical screen or a modified one to simulate a lack of a correct accommodation cue. The range of considered focal distance offsets was 0.2 to 5 diopters. For the screen located at 0.25 m, we moved the virtual object further from the observer, while for the screen located at 5.0 m, we moved the virtual image closer to the observer.

5.2 Participants

Twelve subjects (2 F, 10 M, 20 to 34 years of age) that had a normal or corrected-to-normal vision, took part in the experiment. To keep participants inside the eyebox of our NED, all participants used a chin and forehead rest.

5.3 Procedure

At each trial, a participant was asked to monocularly fixate at one of the physical screens. To this end, a simple math equation was displayed on the screen using a font of height 15 arcmin, while nothing was displayed on our NED. The user was asked to push one button if the equation was true and another if it was false. This math task was introduced to control the user fixation and give him enough time to correctly accommodate to the distance at which the physical screen was located. Immediately after responding, the stimulus appeared on the reference and the NED at a location central to the equation. The presentation time of the stimulus was set to 300 ms. The time was chosen such that it was just-enough to perform the visual acuity task, and it was determined during a pilot experiment. Note that the time is also shorter than the latency before the actual change in the lens shape is triggered, which we discuss in more details in Section 6. Next, the participant was presented with a blank screen and asked to press a button selecting whether the two patterns were of equal or different orientation. Afterwards, the study continued with a next trial. In total, two physical displays and six focus distances for the NED were used in random order which after 20 repetitions gave the total of 240 trials per participant. Each participant took on average 30 minutes to complete the task.

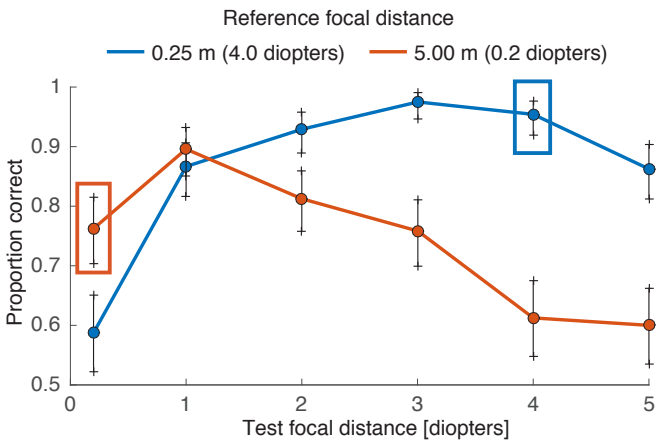

Fig. 11. The proportion correct as a function of test focal distance of the NED. Two points marked by rectangles are points where the reference and the test distances matched. For such conditions, the performance is expected to be the best. The error bars denote Clopper-Pearson binomial confidence intervals.

5.4 Results

The graph in Figure 11 shows the relation of the NED focal distance and the proportion of correct responses for each of the reference displays. We performed a χ^2-test to analyze differences between different conditions and found a significance influence of the test focal distance on the proportion correct for both 0.2 diopters ($\chi^2 = 82.7, df = 5, p < 0.001$) and 4.0 diopters ($\chi^2 = 204.7, df = 5, p < 0.001$) references. A post-hoc analysis with Bonferoni correction and significance level equal to 0.05 revealed that the differences between test pairs were significant for all but the following: 0.2/2.0, 0.2/3.0, 2.0/3.0, 4.0/5.0 for 0.2 diopters reference and 1.0/2.0, 1.0/5.0, 2.0/4.0, 3.0/4.0 for 4.0 diopters reference.

In general, as the test focal distance approached the reference depth, i.e., both stimuli were presented at the the same focal distance, the participants were able to correctly perform the task more often maxing out at 97.5% and 89.6% for stimuli at 0.25 m (4 diopters) and 5.0 m (0.2 diopters), respectively. The best performance should be located at the points corresponding to the cases where the test and the references focal distances match (see rectangles in Figure 11). This can be observed well for the closer physical display. For the further screen, the drop of the performance for the isofocal condition can be explained by a degradation of the image quality due to a strong membrane distortion compensation required for such an extreme focus depth. This made the comparison of relatively small shapes difficult. Except for this particular case, the trend in our measured data follows the expectation, i.e., the participant performance drops with increasing optical focus difference between both displays.

For the reference display at 0.25 m distance (4 diopters, blue) and our NED set up to focus at 1.00 m (1 diopter) participants had to compare two shapes at focal distances differing by 3.0 diopters and had a mean performance of 86.7%. As our analysis shows, this is a significant drop from the optimal performance when the focus for NED matches the physical screen. Similar observations can be made for the reference display at distance of 5.00 m (0.2 diopters, red), where the performance significantly drops to 75.8% for the NED focused at 0.33 m (3 diopters) when compared to the case of focusing it at 1.0 m (1 diopters). Situations like these occur while using current AR displays with fixed focus distance. From these results, we conclude that the varifocal properties of our device allow improving the user performance in tasks that require simultaneous observation of the virtual and the real worlds.

6 Limitations

6.1 Pneumatics:

The response time of 300 ms for switching from one extreme depth level to an another can be shortened by revisiting our pneumatics hardware design. Through our early experimentation, we found out that including a solenoid controlled bleed hole leads to 100 ms response time. We believe that the response time can be decreased further with a design that has two vacuum compartments rather than one. Pneumatics of our prototype creates low volume audible noise as it accommodates to different image planes. A two-compartments-based design can also help us to avoid noise through vacuum. Our current peripheral devices that regulate our pneumatics can also be smaller in volume by using custom regulators. We are willing to overcome the mentioned design challenges in our next iterations by redesigning our pneumatics structure accordingly.

6.2 Form-factor:

Our current optical design can be less bulky in size. According to our ray tracing model, tilting deformable membrane mirror towards peripheral can shrink the size of required aperture size towards peripheral. Working with circular apertures can also help us to avoid usage of lenses to correct astigmatism introduced by elliptical aperture shape used in our prototype. Through such modifications aperture size can be smaller in volume, leading to more practical implementations. Another challenge to be addressed is shrinking the optical path in between a display and a deformable membrane mirror, $d_{display}$. Through our analysis, with an increasing $d_{display}$, we observe that display size grows, and the supported resolution increases. We are planning to address this challenge in the near future by revisiting the display side of our design with a per eye display module with additional static custom optics. We will be iterating our current prototype to a more optimal point through off-the-shelf offerings, so that a wearable version can also be realized for further experimentation towards AR application specific research.

6.3 Latency:

The performance of our display is affected by the system latency. Its first source is the eye-tracking system. However, it has been demonstrated that good quality eye-tracking systems [9], can achieve latency as low as 50 ms.

The second source of latency is the membrane. The change of its shape for the most extreme scenario can take up to 300 ms. Again, these limitations may remain unnoticed due to the characteristic of the eye accommodation process which also exhibits large delays. First, a latency (reaction time) in the range of $300-500$ ms has typically been observed before the actual change in the lens shape is initiated [4,6,10,36]. While Phillips et al. [36] have observed latencies as short as 200 ms, the probability of their occurrence is very low. They hypothesize that such short latencies can be explained by coincidence or confusion of some subjects who have not carefully followed the experiment protocol. The duration of actual lens accommodation of $500-800$ ms has been reported [4, 6, 10, 36], which means that the complete accommodation cycle, including the latency, typically requires around 1 second [6]. The velocity of accommodation is a good measure of the lens accommodation dynamics. Bharadwaj et al. [4] observed a smooth increase in velocity to its peak value and then its slightly slower reduction to a steady state. The peak velocity increased with the accommodation magnitude and the highest value of around 10 diopters/second has been reported. Kasthurirangan et al. [17] observed a similar average peak velocity for the lens accommodation, but a high variance can be observed in their data. Also, for disaccommodation, the peak velocities over 20 diopters/second have been measured for the large accommodation magnitudes of $4-5$ diopters, which are still within the range of focal changes in our NED. The operational velocity of our membrane amounts to 16.6 diopters/second, which might be below the peak velocity for disaccommodation in extreme depth changes. Since our membrane deformation is initiated during the period of eye accommodation latency and its maximum duration is less than 300 ms, we expect that the whole process is completed well before such extreme lens accommodation velocities are reached.

The total latency of our system remains below the delays of the eye accommodation process and may be sufficiently low for AR applications. This is supported by results of our subjective experiments. We leave more in-depth experiments regarding latency requirements

for future work. Note that in contrast to the discussed findings from the perception literature here, the dynamic accommodation state in our setup is affected by simultaneously changing shapes of the NED's membrane and eye's lens, which has not been investigated so far.

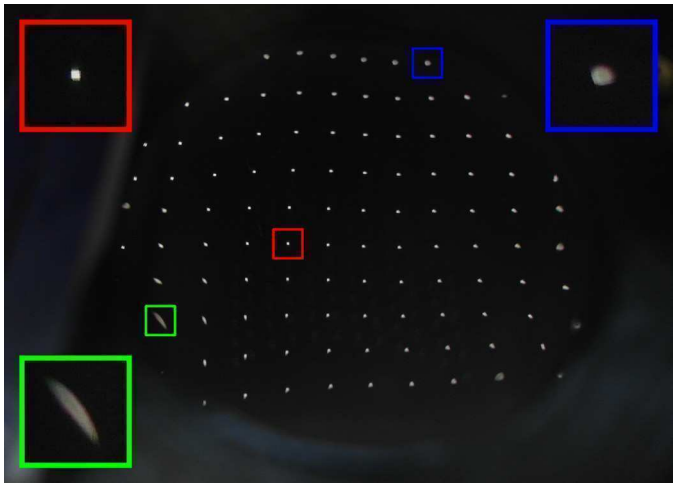

Fig. 12. A view approximating the point spread function across the membrane. Squares of 3x3 pixels are illuminated in a grid pattern to show the graceful degradation of focus across the membrane. Central region shows minimal point spread (red inset), while periphery shows a much larger point spread (blue inset). Severe defocus in lower left region (green inset) is caused by inadequate tension on membrane when closing and securing the housing.

6.4 Consistency of focal properties:

Our display does not guarantee the same focus properties across the entire field of view as this would require a more challenging membrane design, i.e., optimizing its mechanical properties. Instead, our system provides a correct focal cue in the central vision and its graceful degradation towards peripheral vision as seen in Figure 12. This is aligned with the limitation of the human visual system regarding the accommodation. The perceptual sensitivity to lack of focus is characterized by the eye depth-of-focus (DoF), which denotes the maximum range of retinal defocus that does not cause perceivable blur. The DoF depends on many factors such as the pupil size, the quality of eye optics, as well as properties of observed content in terms of color and contrast, luminance levels, and spatial frequency content [41]. However, typically the DoF at the fovea is considered, and values around 0.3 diopters have been reported [5] for suprathreshold contrasts and photopic lighting conditions. Note that the accommodative system responds to much smaller focal changes of 0.12 diopters, but those are not perceivable [21]. With increasing retinal eccentricity the DoF increases significantly [35, 40]. Even in the relatively near retinal periphery of 5°, it amounts to 2.5 diopters. DoF saturates at the level of 6-7 diopters for eccentricities larger than 30°. The increase of DoF with eccentricity reduces requirements imposed on the membrane design in our display, as relatively high defocus blur can be tolerated outside the central foveal region without causing any perceivable degradation of the image quality. Using the eye tracking system, we are able to provide a precise focus in the fovea region, while the precision of membrane shaping outside such region can be relaxed. This greatly simplifies maintaining the high visual quality over a wide FOV.

6.5 Depth of field:

Our display is capable of displaying only a single depth at a time, which leads to incorrect views for virtual content at different depths. A simple solution to this would be to apply a defocus kernel approximating the eye's point spread function to the virtual image according to the depth of the virtual objects. Due to the potential of rendered blur not being equivalent to optical blur, we have not implemented this solution. Future work must evaluate the effectiveness of using rendered blur in place of optical blur.

6.6 Occlusion support:

The work of Kiyokawa et al. [20] describes an occlusion cable NED, and introduces an application space that requires occlusion support. Our proposal does not attempt to support occlusion. We leave this challenge as a future work.

6.7 Monocular vs. binocular experiment:

We present a binocular display, but verify it only by a monocular experiment. Our monocular experiment has demonstrated that combined real-virtual depth-varying task performance can be improved with focal accommodation. However, binocular experiments would allow us to show a relationship between vergence-accommodation conflict and task performance. We leave binocular experiments for a future work, and are excited by the possible perceptual studies which are now open with this new hardware prototype. In particular, we would like to verify that visual fatigue due to vergence accommodation conflict can be mitigated by our display. Such experiments can potentially also reveal more interesting facts about the vergence-accommodation relationship.

7 Conclusion

In order to provide a high-quality augmented reality experience, it is crucial to design headsets that are capable of reproducing all visual cues across whole visual field. In this respect, the most challenging are reproduction of accommodation cue as well as providing wide field of view. To address these problems, we propose a novel design of a see-through near-eye display for augmented reality applications. The key to our solution are two membranes with half-mirror properties. Thanks to their deformation properties, their focal power can be adjusted using an airtight chamber to provide accommodation cues matching the observer's fixation distance determined by an eye tracker. This addresses the problem of visual discomfort which is usually caused by a mismatch between vergence and accomodation. It also improves user task performance as demonstrated in our experiment. Another unique advantage of our membranes is the fact that they enable a significantly larger field of view when compared to other varifocal designs. Despite few limitations of our system, we believe that providing correct focus cues as well as wide field of view are most crucial features of head-mounted displays that try to provide seamless integration of the virtual and the real world. Our screen not only provides basis for new, improved designs, but it can be directly used in perceptual experiments that aim at determining requirements for future systems. We, therefore, argue that our work will significantly facilitate the development of augmented reality technology and contribute to our understanding of how it influences user experience.

Acknowledgments

The authors wish to thank Joohwan Kim, Ward Lopes, Josef Spjut, and Turner Whitted for fruitful discussions. Jim Mahaney was invaluable in consulting and assisting with the physical set-up of our display prototype. The authors would also like to thank the participants of our subjective experiments for their participation, and the anonymous reviewers for valuable feedback.

This work was partially supported by National Science Foundation (NSF) Grant IIS-1645463 "EAGER: Wide Field of View Augmented Reality Display with Dynamic Focus," by NSF grant A14-1618-001 "II-New: Seeing the Future: Ubiquitous Computing in EyeGlasses," by a grant from NVIDIA Research, by the Fraunhofer and Max Planck cooperation program within the German pact for research and innovation (PFI), and by the BeingTogether Centre, a collaboration between Nanyang Technological University (NTU) Singapore and University of North Carolina (UNC) at Chapel Hill, supported by UNC and the Singapore National Research Foundation, Prime Minister's Office, Singapore under its International Research Centres in Singapore Funding Initiative.

REFERENCES

[1] K. Akşit, J. Kautz, and D. Luebke. Slim near-eye display using pinhole aperture arrays. *Applied optics*, 54(11):3422–3427, 2015.

[2] K. W. Arthur. *Effects of field of view on performance with head-mounted displays*. PhD thesis, University of North Carolina at Chapel Hill, 2000.

[3] H. Benko, E. Ofek, F. Zheng, and A. D. Wilson. Fovear: Combining an optically see-through near-eye display with projector-based spatial augmented reality. In *Proceedings of the 28th Annual ACM Symposium on User Interface Software & Technology*, pages 129–135. ACM, 2015.

[4] S. R. Bharadwaj and C. M. Schor. Acceleration characteristics of human ocular accommodation. *Vision Research*, 45(1):17–28, 2005.

[5] F. Campbell. The depth of field of the human eye. *Optica Acta: International Journal of Optics*, 4(4):157–164, 1957.

[6] F. Campbell and G. Westheimer. Dynamics of accommodation responses of the human eye. *J. Physiol.*, 151(2):285–295, 1960.

[7] J. Carmigniani, B. Furht, M. Anisetti, P. Ceravolo, E. Damiani, and M. Ivkovic. Augmented reality technologies, systems and applications. *Multimedia Tools and Applications*, 51(1):341–377, 2011.

[8] N. A. Dodgson. Variation and extrema of human interpupillary distance. In *Electronic imaging 2004*, pages 36–46. International Society for Optics and Photonics, 2004.

[9] B. Guenter, M. Finch, S. Drucker, D. Tan, and J. Snyder. Foveated 3d graphics. *ACM Transactions on Graphics (TOG)*, 31(6):164, 2012.

[10] G. Heron, W. Charman, and C. Schor. Dynamics of the accommodation response to abrupt changes in target vergence as a function of age. *Vision Research*, 41(4):507 – 519, 2001.

[11] D. M. Hoffman, A. R. Girshick, K. Akeley, and M. S. Banks. Vergence–accommodation conflicts hinder visual performance and cause visual fatigue. *Journal of vision*, 8(3):33–33, 2008.

[12] X. Hu and H. Hua. High-resolution optical see-through multi-focal-plane head-mounted display using freeform optics. *Optics express*, 22(11):13896–13903, 2014.

[13] H. Hua and B. Javidi. A 3d integral imaging optical see-through head-mounted display. *Optics express*, 22(11):13484–13491, 2014.

[14] F.-C. Huang, D. Luebke, and G. Wetzstein. The light field stereoscope. *ACM SIGGRAPH Emerging Technologies*, page 24, 2015.

[15] P. V. Johnson, J. A. Parnell, J. Kim, M. S. Banks, G. D. Love, et al. Assessing visual discomfort using dynamic lens and monovision displays. In *3D Image Acquisition and Display: Technology, Perception and Applications*, pages TT4A–1. Optical Society of America, 2016.

[16] P. V. Johnson, J. A. Parnell, J. Kim, C. D. Saunter, G. D. Love, and M. S. Banks. Dynamic lens and monovision 3d displays to improve viewer comfort. *arXiv preprint arXiv:1512.09163*, 2015.

[17] S. Kasthurirangan, A. S. Vilupuru, and A. Glasser. Amplitude dependent accommodative dynamics in humans. *Vision Research*, 43(27):2945 – 2956, 2003.

[18] H.-J. Kim, S.-K. Lee, M.-L. Piao, N. Kim, and J.-H. Park. Three-dimensional holographic head mounted display using holographic optical element. In *Consumer Electronics (ICCE), 2015 IEEE International Conference on*, pages 132–133. IEEE, 2015.

[19] K. Kiyokawa. A wide field-of-view head mounted projective display using hyperbolic half-silvered mirrors. In *Proceedings of the 2007 6th IEEE and ACM International Symposium on Mixed and Augmented Reality*, pages 1–4. IEEE Computer Society, 2007.

[20] K. Kiyokawa, M. Billinghurst, B. Campbell, and E. Woods. An occlusion-capable optical see-through head mount display for supporting co-located collaboration. In *Proceedings of the 2nd IEEE/ACM International Symposium on Mixed and Augmented Reality*, page 133. IEEE Computer Society, 2003.

[21] J. C. Kotulak and C. M. Schor. The accommodative response to subthreshold blur and to perceptual fading during the troxler phenomenon. *Perception*, 15(1):7–15, 1986.

[22] G. Kramida. Resolving the vergence-accommodation conflict in head-mounted displays. *IEEE Transactions on Visualization and Computer Graphics*, 22(7):1912–1931, 2016.

[23] E. Kruijff, J. E. Swan II, and S. Feiner. Perceptual issues in augmented reality revisited. In *ISMAR*, volume 9, pages 3–12, 2010.

[24] D. Lanman and D. Luebke. Near-eye light field displays. *ACM Transactions on Graphics (TOG)*, 32(6):220, 2013.

[25] S. Lee, X. Hu, and H. Hua. Effects of optical combiner and ipd change for convergence on near-field depth perception in an optical see-through hmd. *IEEE transactions on visualization and computer graphics*, 22(5):1540–1554, 2016.

[26] G. Lippmann. Epreuves reversibles. photographies integrals. *Comptes-Rendus Academie des Sciences*, 146:446–451, 1908.

[27] S. Liu, D. Cheng, and H. Hua. An optical see-through head mounted display with addressable focal planes. In *Mixed and Augmented Reality, 2008. ISMAR 2008. 7th IEEE/ACM International Symposium on*, pages 33–42. IEEE, 2008.

[28] A. Maimone, D. Lanman, K. Rathinavel, K. Keller, D. Luebke, and H. Fuchs. Pinlight displays: wide field of view augmented reality eyeglasses using defocused point light sources. In *ACM SIGGRAPH 2014 Emerging Technologies Booth 203*. ACM, 2014.

[29] J. D. Mansell, S. Sinha, and R. L. Byer. Deformable mirror development at stanford university. In *International Symposium on Optical Science and Technology*, pages 1–12. International Society for Optics and Photonics, 2002.

[30] S. McKay, G. M. Mair, S. Mason, and K. Revie. Membrane-mirror-based autostereoscopic display for tele-operation and teleprescence applications. In *Electronic Imaging*, pages 198–207. International Society for Optics and Photonics, 2000.

[31] S. McKay, S. Mason, L. S. Mair, P. Waddell, and S. M. Fraser. Membrane-mirror-based display for viewing 2d and 3d images. In *Electronic Imaging'99*, pages 144–155. International Society for Optics and Photonics, 1999.

[32] H. Nagahara, Y. Yagi, and M. Yachida. Super wide field of view head mounted display using catadioptrical optics. *Presence*, 15(5):588–598, 2006.

[33] G. W. R. Konrad, E.A Cooper. Novel optical configurations for virtual reality: Evaluating user preference and performance with focus-tunable and monovision near-eye displays. *Proceedings of the ACM Conference on Human Factors in Computing Systems (CHI'16)*, 2016.

[34] E. G. Rawson. Vibrating varifocal mirrors for 3-d imaging. *IEEE Spectrum*, 6(9):37–43, 1969.

[35] L. Ronchi and G. Molesini. Depth of focus in peripheral vision. *Ophthalmic Res*, 7(3):152–157, 1975.

[36] P. S., D. Shirachi, and S. L. Analysis of accommodative response times using histogram information. *American Journal of Optometry & Archives of American Academy of Optometry*, 49(5):389–400, 1972.

[37] R. Seghir and S. Arscott. Extended pdms stiffness range for flexible systems. *Sensors and Actuators A: Physical*, 230:33–39, 2015.

[38] A. Sisodia, A. Riser, and J. R. Rogers. Design of an advanced helmet mounted display (ahmd). In *Defense and Security*, pages 304–315. International Society for Optics and Photonics, 2005.

[39] G. Spencer and M. Murty. General ray-tracing procedure. *JOSA*, 52(6):672–676, 1962.

[40] B. Wang and K. J. Ciuffreda. Depth-of-focus of the human eye in the near retinal periphery. *Vision Research*, 44(11):1115 – 1125, 2004.

[41] B. Wang and K. J. Ciuffreda. Depth-of-focus of the human eye: Theory and clinical implications. *Survey of Ophthalmology*, 51(1):75 – 85, 2006.

[42] A. Werber and H. Zappe. Tunable pneumatic microoptics. *Journal of Microelectromechanical Systems*, 17(5):1218–1227, 2008.

[43] S. Yamazaki, M. Mochimaru, and T. Kanade. Simultaneous self-calibration of a projector and a camera using structured light. In *Proc. Projector Camera Systems*, pages 67–74, 2011.